h/e Magnetic Flux Modulation of the Energy Gap in Nanotube Quantum Dots

Ulas C. Coskun, Tzu-Chieh Wei, Smitha Vishveshwara, Paul M. Goldbart, Alexey Bezryadin*

We report experiments on quantum dot single-electron-tunneling (SET) transistors made from short multiwall nanotubes and threaded by magnetic flux. Such systems allow us to probe the electronic energy spectrum of the nanotube and its dependence on the magnetic field. Evidence is provided for the interconversion between gapped (semiconducting) and ungapped (metallic) states. Our tubes exhibit *h/e*-period magnetic flux dependence, in agreement with simple tight-binding calculations.

Carbon nanotubes (*1*–*3*) can be metallic or semiconducting, depending on their chirality, i.e., the manner in which their constituent graphene sheets are rolled and seamed (*4*–*9*). The chirality cannot be altered at will. However, theoretical analysis (*10*–*12*) shows that a coaxial magnetic field, and thus Aharonov-Bohm (AB) (*13*) flux, can change the electronic properties of a given nanotube and convert it from metallic to semiconducting and vice versa. Multiwall carbon nanotubes (MWNTs), unlike most other single molecules, have the ideal size and structure for studying the effect of the AB flux on the energy spectrum and conduction properties. Being concentric cylinders with an outer radius $R \approx 15$ nm, they allow penetration by an entire flux quantum $\Phi_0 = h/e$ (where h is Planck's constant and e is elementary charge) at accessible magnetic fields of about $\Phi_0/\pi R^2 \approx 5.8$ T. Previous experiments (*14*, *15*) indicate that only the outermost shell contributes to conduction. The AB effect has been observed previously in MWNTs (*14*), in the context of linear conductance measurements performed on tubes longer than the phase-breaking length. Conductance oscillations reflect the sensitivity of weak localization effects to the AB flux threading the tube, typically yielding an $h/2e$ period (*14*, *16*), although other periods have also been observed (*14*, *17*, *18*). We use tubes shorter than the dephasing length to probe a qualitatively different phenomenon, namely, the electronic energy spectrum modulation by a coaxial magnetic field. This phenomenon is qualitatively similar to the Little-Parks oscillations observed in hollow cylinder–shaped superconductors (*19*). The spectrum is studied by means of differential conductance measurements at finite bias on a single-electron tunneling transistor formed by the nanotube acting as a coherent Coulomb island. Such measurements enable us to observe the flux-induced interconversion of gapped and ungapped nanotube energy spectra, and thus the interconversion of semiconducting and metallic nanotubes.

The samples are fabricated on a Si wafer covered with 500-nm SiO_2 and a 60-nm SiN films. A 100-nm trench is etched into SiN film, and an undercut is created by HF wet etching. A strip of gold is then evaporated across the trench, thus forming a pair of closely spaced Au electrodes, later used as source and drain. We position an individual MWNT (*20*) over both electrodes, to create a single-electron tunneling (SET) transistor (*21*) (Fig. 1A). During the measurements, a gate voltage (V_g) is applied to the Si wafer, which is strongly doped and conducting. The bias voltage (V_B) is applied between the pair of Au electrodes. Two samples, A and B, of respective lengths $L_A = 800$ nm and $L_B = 500$ nm and radii $R_A = 15 \pm 1$ nm and $R_B = 13 \pm 1$ nm, were investigated, both showing SET behavior and an *h/e* response to the magnetic flux. A representative scanning electron micrograph of a nanotube-based SET transistor is shown in Fig. 1B.

The samples are initially probed by applying a small-amplitude (≈0.05 mV, 7 Hz) ac voltage bias between the source and the drain, for a range of gate voltages, and by measuring the resulting ac current. These initial test measurements are done at $T = 0.3$ K (Fig. 1, C and E). Figure 1C shows a typical conductance variation versus gate voltage; Fig. 1E presents a color-coded differential conductance map plotted against the gate and bias voltages for our

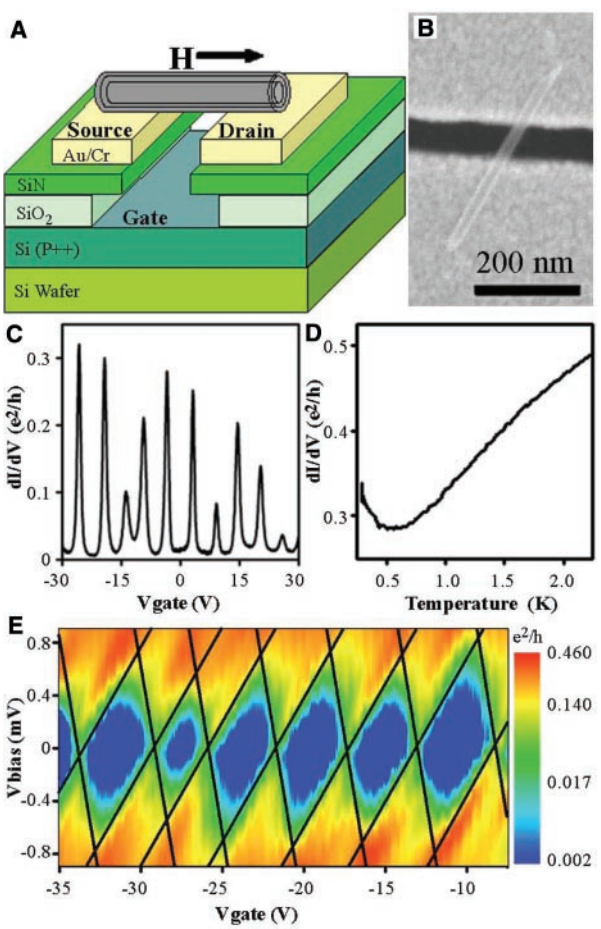

Fig. 1. Fabrication and measurements on quantum dot devices made of nanotubes. (**A**) Schematic of a single-electron transistor built from a single nanotube. Multiwall carbon nanotubes (*20*) are deposited onto the Au electrodes from a dichloroethane solution. Magnetic field is parallel to the tube axis. (**B**) A representative SEM image of a sample (sample B). (**C**) An example of a sequence of quasi-periodic Coulomb conductance peaks for our nanotube SET transistor. (**D**) Temperature dependence of the normalized conductance of one of the Coulomb peaks. The increasing conductance suggests resonant tunneling through extended single energy levels. (**E**) Coulomb blockade diamond measured on sample A ($B = 9$ T).

Department of Physics, University of Illinois at Urbana-Champaign, 1110 West Green Street, Urbana, IL 61801–3080, USA.

*To whom correspondence should be addressed. E-mail: bezryadi@uiuc.edu

nanotube SET transistors (in this case, a constant voltage bias was applied in addition to the ac bias). In the Coulomb blockade regime, observed similarly in both samples, the conduction through the tube at low bias voltage occurs only at those specific values of the gate voltage for which it is comparably probable to have N or $N + 1$ electrons on the tube, resulting in the expected Coulomb blockade conductance peaks (*22*) shown in Fig. 1C. The gate-voltage differences between Coulomb peaks are proportional to $E_C + \Delta E$ —the sum of the charging energy and the single–particle level spacing. The pattern of Coulomb blockade diamonds (*23*) in Fig. 1E is a typical feature observed on SET devices, which occurs as a result of single-electron transport. Because the distance between the corners of the Coulomb diamonds in the V_B direction is roughly $2E_C$ (if the level splitting is neglected), we determine that $E_{CA} \approx 0.4$ meV and $E_{CB} \approx 0.6$ meV for samples A and B, respectively. These values are comparable to an estimate of the charging energy of a nanotube, $E_C \approx 1.4$ eV/L (nm) (*24*), which gives 1.75 meV and 2.8 meV for samples A and B, respectively. In both cases, the measured E_C is lower than that estimated, possibly due to a strong capacitive coupling of the nanotube to the electrodes. The temperature dependence of the Coulomb peak height (Fig. 1D) shows an increase with decreasing temperature. This feature is observed on some but not all Coulomb peaks and indicates quantum dot behavior, when resonant tunneling occurs through individual electronic states, extended in the nanotube from the source to the drain electrodes (*22*). The increase begins at $T \sim 0.5$ K, indicating that the level spacing is about 0.05 meV or larger.

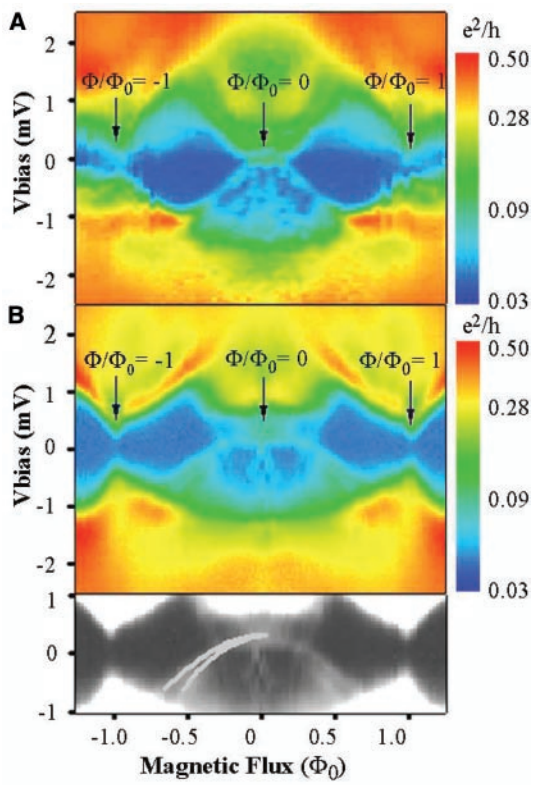

Fig. 2. Color-coded differential conductance of two MWNT quantum dots plotted against bias voltage and magnetic flux. (**A**) Sample A differential conductance was measured at a Coulomb peak (in zero field) with fixed $V_g = -4.1$ V. (**B**) Sample A differential conductance was measured slightly off a Coulomb peak, with fixed $V_g = -35$ V. The inset shows the same data in black-and-white format in order to emphasize the Zeeman splitting of a single energy level. The gray lines are guides to the eye, marking the split levels. The image is symmetric with respect to the sign change of the magnetic field.

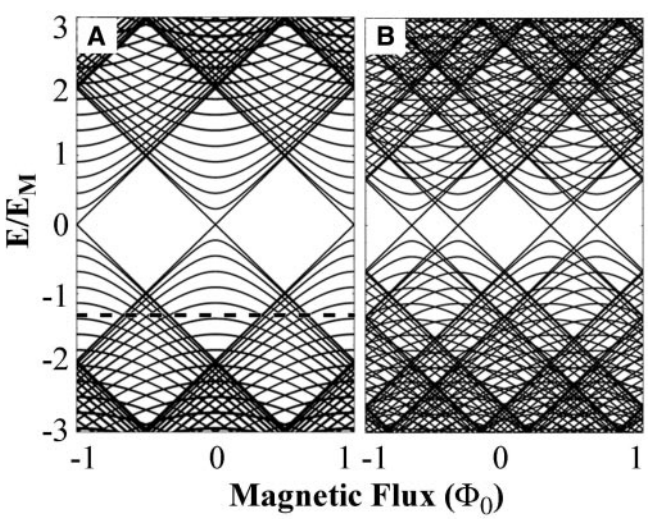

Fig. 3. Energy levels for nanotubes plotted against magnetic flux threaded through the nanotube. The simulations are done for two 730-nm-long tubes of different chiralities: (**A**) (200,200) armchair and (**B**) (346, 0) zigzag (the diameter of both tubes is 28 nm). The energy scale is in units of E_M (see text). The dispersions are calculated within the standard single-particle tight-binding model (*26*). A dashed horizontal line in (A) indicates a possible position of the Fermi level for sample B, shifted by doping from the half-filling condition (*25*).

We now discuss the response of sample A to the magnetic flux in detail (*25*). Our main results are displayed as color-coded maps of the differential conductance, plotted against bias voltage and magnetic flux in Fig. 2, A and B. The flux, $\Phi = \pi R^2 B$, is calculated from the applied magnetic field, B, and the measured outer radius. The gate voltage is kept constant during each measurement. The resulting conductance maps are always symmetric with respect to the magnetic field sign change. Two measurements are shown: for $V_g = -4.1$ V (Fig. 2A), corresponding to the maximum of one of the Coulomb peaks at zero flux and zero bias, and for $V_g = -35$ V (Fig. 2B), which is slightly off another (zero-flux, zero-bias) maximum. These measurements show the same trend: The conductance gap (i.e., the blue region, where the conductance is very low) continues to widen with increasing magnitude of the AB flux, starting small until a half-flux quantum is reached. Beyond half-flux quantum, the trend reverses until a full-flux quantum is reached, at which point the induced gap reaches a pronounced minimum. The conductance map of sample B (fig. S1) also exhibits a distinct h/e magnetic flux periodicity, with a shift of the pattern by half-flux quantum with respect to sample A (i.e., maxima and minima are interchanged).

To understand the origin of the field-induced gap structure and related features of the conductance maps, we have compared them with predictions of a simple tight-binding model for the π-electrons of carbon nanotubes of finite length (*7*, *26*). Summarized in Fig. 3, these show a variation, with magnetic flux, of the low-lying single-particle energy levels for (A) a metallic armchair tube and (B) a semiconducting zigzag tube. The most prominent feature is the variation, and even creation, of a gap induced by the magnetic flux with period h/e (the gap is the diamond-shaped region from which all lines are expelled). For metallic tubes, the magnetic flux opens a gap and results in a sequence of identical gap diamonds; this gap closes at integral flux quanta. By contrast, for semiconducting tubes, magnetic flux tends to shrink the gap, leading to gap closure at pairs of flux values straddling half-flux quanta, resulting in gap diamonds of two distinct sizes. A simple band-structure estimate of the maximum field-induced (me-

tallic case) gap gives $2E_M = \sqrt{3}ta/(2R) = 36$ meV, where $a \approx 2.49$ Å is the lattice constant and $t \approx 2.5$ eV is the intersite hopping amplitude for graphene. In general, E_M is always comparable in scale to that of a chirality-induced gap in a nanotube of the same radius.

To compare the experimental differential conductance maps and the theoretical predictions, we note that the former are essentially a measure of density of electronic states at an energy given by the bias voltage. Figure 3 also characterizes this quantity, inasmuch as the density of lines reflects the density of states. We see from Fig. 2, A and B, that our measurements qualitatively resemble the broad predictions shown in Fig. 3A, calculated for a metallic tube. The resemblance suggests that the outer shell of sample A is intrinsically metallic. On the other hand, sample B (fig. S1) shows a similarity with simulations of semiconducting tubes (Fig. 3B), or possibly metallic and strongly doped tubes, with the Fermi level (dashed line in Fig. 3A) shifted away from the half-filled position as a result of doping. In both samples, the observed maximum gap is about an order of magnitude smaller than the estimated value $E_M = 18$ meV. Possible explanations for this include doping by impurities and intershell coupling, which can also introduce effective disorder (*16*, *27*).

Zeeman splitting can also be observed on our SET devices, confirming the quantum dot behavior (Fig. 2B, black-and-white inset). Here we see a single energy level, which splits in the magnetic field by an amount that agrees with the *g*-factor reported previously for single-wall nanotubes (*22*). Indeed, consider, for instance, the splitting at $\Phi = 0.5\Phi_0$ (which corresponds to a field of 2.9 T), which is about 0.32 meV. This translates into a *g*-factor of 1.95, in agreement with previous reports (*22*). From these data, it is possible to estimate that the Zeeman splitting expected for $B \sim 10$ T roughly equals the maximum experimentally observed gap (0.5 to 1 meV). This explains the observation that the gap structure is not periodic with flux. This effect is clearly seen in Fig. 2A, where the periodicity with flux breaks down at high fields. Further understanding of the interplay between magnetic field–induced Zeeman and orbital effects are yet to be achieved by carrying out measurements at temperatures of a few millikelvins.

References and Notes

1. S. Iijima, *Nature* **354**, 56 (1991).
2. S. Iijima, T. Ishihashi, *Nature* **363**, 603 (1993).
3. T. W. Ebbesen *et al.*, *Nature* **382**, 54 (1996).
4. J. W. Mintmire, B. I. Dunlap, C. T. White, *Phys. Rev. Lett.* **68**, 631 (1992).
5. R. Saito, M. Fujita, G. Dresselhaus, M. S. Dresselhaus, *Appl. Phys. Lett.* **60**, 2204 (1992).
6. C. L. Kane, E. J. Mele, *Phys. Rev. Lett.* **78**, 1932 (1997).
7. R. Saito, G. Dresselhaus, M. S. Dresselhaus, *Physical Properties of Carbon Nanotubes* (Imperial College, London, 1998).
8. J. W. G. Wildoer, L. C. Venema, A. G. Rinzler, R. E Smalley, C. Dekker, *Nature* **391**, 59 (1998).
9. T. W. Odom, J.-L. Huang, P. Kim, C. M. Lieber, *Nature* **391**, 62 (1998).
10. S. Roche, G. Dresselhaus, M. S. Dresselhaus, R. Saito, *Phys. Rev. B* **62**, 16092 (2000).
11. H. Ajiki, T. Ando, *J. Phys. Soc. Jpn.* **62**, 1255 (1993).
12. J. P. Lu, *Phys. Rev. Lett.* **74**, 1123 (1995).
13. Y. Aharonov, D. Bohm, *Phys. Rev.* **115**, 485 (1959).
14. A. Bachtold *et al.*, *Nature* **397**, 673 (1999).
15. S. Frank, P. Poncharal, Z. L. Wang, W. A. de Heer, *Science* **280**, 1744 (1999).
16. S. Roche, F. Triozon, A. Rubio, D. Mayou, *Phys. Rev. B* **64**, 121401 (2001).
17. J.-O. Lee *et al.*, *Solid State Commun.* **115**, 467 (2000).
18. A. Fujiwara, K. Tomiyama, M. Yumura, K. Uchida, H. Suematsu, *Phys. Rev. B* **60**, 13492 (1999).
19. W. A. Little, R. D. Parks, *Phys. Rev. Lett.* **9**, 9 (1962).
20. Alfa Aesar, Multiwall nanotubes, Stock #43197, Lot #L03J42.
21. L. P. Kouwenhoven *et al.*, in *Mesoscopic Electron Transport*, L. L. Sohn, L. P. Kouwenhoven, G. Schön, Eds. (Kluwer, Boston, 1997), pp. 105–214.
22. S. J. Tans *et al.*, *Nature* **386**, 474 (1997).
23. H. Grabert, M. H. Devoret, Eds., *Single Charge Tunneling* (Plenum, New York, 1992).
24. M. Bockrath *et al.*, *Science* **275**, 1922 (1997).
25. The details for sample B are provided as supporting material in *Science* Online.
26. H. Ajiki, T. Ando, *J. Phys. Soc. Jpn.* **65**, 505 (1996).
27. T. Ando, *Semicond. Sci. Techol.* **15**, R13 (2000).

28. We acknowledge the technical assistance of J. Hughes and support from NSF (grant EIA01-21568), the U.S. Department of Energy (DOE) (grant DEFG02-96ER45434), and the Sloan Research Fellowship. The fabrication was done at the Frederick Seitz Materials Research Laboratory supported by DOE (grant DEFG02-91-ER45439).

Supporting Online Material

www.sciencemag.org/cgi/content/full/304/5674/1132/DC1
SOM Text
Fig. S1
References

10 February 2004; accepted 19 April 2004

Infrared Spectroscopic Evidence for Protonated Water Clusters Forming Nanoscale Cages

Mitsuhiko Miyazaki, Asuka Fujii,* Takayuki Ebata, Naohiko Mikami*

Size-dependent development of the hydrogen bond network structure in large-sized clusters of protonated water, $H^+(H_2O)_n$ (n = 4 to 27), was probed by infrared spectroscopy of OH stretches. Spectral changes with cluster size demonstrate that the chain structures at small sizes ($n \lesssim 10$) develop into two-dimensional net structures ($\sim 10 < n < 21$), and then into nanometer-scaled cages ($n \geq 21$).

Because of the fundamental importance of protonated water, $H^+(H_2O)_n$ cluster cations have been studied extensively as a microscopic model of protonated water in the condensed phase (*1*–*11*). These studies, however, have been based mainly on mass spectrometry measurements. Although the thermodynamics of $H^+(H_2O)_n$ has been extensively investigated (*3*, *4*), structural information is still very limited, except for the small clusters, $n \leq 8$. Lee, Chang, and their co-workers carried out a detailed structural analysis of protonated water clusters using infrared (IR) spectroscopy and ab initio calculations (*5*–*7*). They determined the most stable structures for the clusters, $n \leq 6$, and they also suggested that the hydrogen bond network would develop from a chain-type structure at small cluster sizes ($n \leq 6$) to a two-dimensional (2D) net-type structure at $n \sim 7$ to 8 (*7*). Such hydrogen bond network structures in the protonated water clusters are substantially different from those of the neutral water clusters, $(H_2O)_n$, which form 3D cage structures even at $n = 6$ (*11*–*13*).

Very few experimental studies on structures of protonated water of $n > 8$ have been carried out. The only exception is the cluster $n = 21$, which is the well-known "magic number" in the mass distribution of $H^+(H_2O)_n$. A regular dodecahedral cage structure encaging one water molecule in the cavity has been proposed (*1*, *2*) with support from ab initio calculations (*9*, *10*), but no direct experimental evidence has been obtained.

We report IR spectra of size-selected protonated water clusters, $H^+(H_2O)_n$, from n = 4 to $n = 27$. The OH stretching vibrational region of the clusters was probed, and the formation of hydrogen-bonded 3D cage structures was demonstrated for the large-sized protonated water of $n \geq 21$.

The IR spectra of the $H^+(H_2O)_n$ cluster ions in the gas phase were measured with the tandem quadrupole mass filter–type spectrometer, described in (*14*), with some modifications for

Department of Chemistry, Graduate School of Science, Tohoku University, Sendai 980-8578, Japan.

*To whom correspondence should be addressed. E-mail: asuka@qclhp.chem.tohoku.ac.jp (A.F.), nmikami@qclhp.chem.tohoku.ac.jp (N.M.)